

Digital Beamforming Enhanced Radar Odometry

Jingqi Jiang¹, Shida Xu^{1,2}, Kaicheng Zhang^{1,2}, Jiyuan Wei¹, Jingyang Wang³ and Sen Wang¹

Abstract—Radar has become an essential sensor for autonomous navigation, especially in challenging environments where camera and LiDAR sensors fail. 4D single-chip millimeter-wave radar systems, in particular, have drawn increasing attention thanks to their ability to provide spatial and Doppler information with low hardware cost and power consumption. However, most single-chip radar systems using traditional signal processing, such as Fast Fourier Transform, suffer from limited spatial resolution in radar detection, significantly limiting the performance of radar-based odometry and Simultaneous Localization and Mapping (SLAM) systems. In this paper, we develop a novel radar signal processing pipeline that integrates spatial domain beamforming techniques, and extend it to 3D Direction of Arrival estimation. Experiments using public datasets are conducted to evaluate and compare the performance of our proposed signal processing pipeline against traditional methodologies. These tests specifically focus on assessing structural precision across diverse scenes and measuring odometry accuracy in different radar odometry systems. This research demonstrates the feasibility of achieving more accurate radar odometry by simply replacing the standard FFT-based processing with the proposed pipeline. The codes are available at [GitHub](#)*

I. INTRODUCTION

Autonomous robots often perceive their environments using a combination of sensors, such as LiDAR [1] and cameras [2], for autonomous navigation. However, these optical sensors tend to be limited by environmental factors, such as adverse weather. In contrast, radio detection and ranging (radar) technology is known for its efficacy in various environmental conditions, being an appealing sensor for autonomous navigation systems.

Among radar systems, Frequency Modulated Continuous Wave (FMCW) millimeter-wave radar systems have gained popularity in autonomous driving applications due to their ability to simultaneously provide distance and, importantly, velocity measurements [3], [4]. However, the excess noise and the low resolution in the Direction of Arrival (DoA) measurements greatly affect the quality of radar detection, degrading the performance of radar-based odometry and SLAM systems. Therefore, in early radar SLAM systems, they primarily used 2D mechanical scanning radar sensors [5]–[8]. These radar sensors employ mechanical spinning mechanisms, similar to LiDAR sensors, to concentrate power

into a narrower beam for increased radar gain and reduced sidelobes, enhancing DoA estimation. However, they are bulky and unable to handle three-dimensional space effectively, which restricts their wide adoption of ground-based autonomous vehicles.

Recently, 4D System-on-Chip (SoC) radar systems have emerged as a promising solution for robotic navigation applications [9]. Without the need for mechanical spinning, these radar systems leverage Multi-Input-Multi-Output (MIMO) technology to estimate a target’s DoA and Doppler information. Additionally, they can be miniaturized into a more compact form factor at a fraction of the cost, facilitating their integration into a wider range of applications. However, the compact size of current SoC radar designs inherently restricts the number of physical antennas that can be accommodated, which reduces the accuracy of DoA and then the performance of radar SLAM.

To alleviate the radar SLAM performance degradation, some works attempted to use multiple radars [10], [11] or fuse other sensors [12]–[15]. However, not only do these approaches fail to resolve the issue of low DoA accuracy fundamentally, but they also lead to more complicated system design and integration with the introduced additional challenges on sensor calibration and synchronization.

Two main directions have been explored in existing literature to address this issue in radar SLAM. The first direction focuses on using multiple sets of antennas from several chips, such as a cascaded 4D SoC radar, to increase aperture. Consequently, the DoA accuracy and the density of the radar point cloud can be improved, opening the door to transfer some LiDAR-based SLAM techniques, like generalized Iterative Closest Point (ICP), point cloud based loop closure [16], and ground segmentation [17], to radar SLAM. However, the cascaded radar solution often results in increased sensor size and power consumption, alongside low frame rate and high computational complexity.

The second direction focuses on enhancing the radar point cloud quality via postprocessing algorithms. Some learning-based methods [18]–[20] utilize LiDAR point clouds as supervision to train models for predicting higher-quality point clouds. Although these methods could improve the quality of point cloud of single-chip mmWave radar, they may not generalize well in environments not being trained and can not provide the Doppler information of point clouds, which is required by most radar odometry/SLAM systems as a critical measurement. As for the non-learning-based methods, Zeng et al. [21] apply the super-resolution techniques (compressed sensing) to the radar signal to realize angular superresolution radar imaging. They show that super-resolution techniques

¹I-X and Department of Electrical and Electronic Engineering, Imperial College London, UK {j.jiang23, s.xu23, k.zhang23, j.wei23, sen.wang}@imperial.ac.uk

²School of Engineering and Physical Sciences, Heriot-Watt University, UK {sx2000, kz13}@hw.ac.uk

³Department of Electronic Engineering, Tsinghua University, China wangjingyang.2019@tsinghua.org.cn

*<https://github.com/SenseRoboticsLab/DBE-Radar>

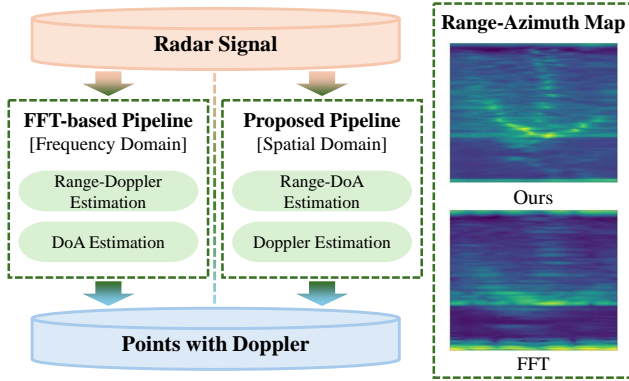


Fig. 1: Comparison of radar signal processing pipelines.

could improve the localization result of occupancy grid map in 2D SLAM. Meiresone et al. [22] utilize a capon-based range-azimuth image generation method before adopting a 2D LiDAR odometry pipeline for radar to estimate the ego-motion of the vehicle. However, neither the learning-based nor model-based methods delve into radar signal processing within the context of radar odometry/SLAM.

Inspired by the significance of feature extraction (i.e., extracting information from image data) in visual SLAM, this work investigates how to leverage raw radar data for radar odometry/SLAM. Fast Fourier Transform (FFT) method is a widely recognized standard practice for processing raw radar data cube [23], due to its ability to quickly transform time-domain signals into the frequency domain for extracting frequency components, such as Doppler shifts and range information. A typical full FFT-based radar signal processing pipeline is illustrated in Figure 1. First, 2D-FFT is performed on the fast-time and the slow-time dimensions, generating range-Doppler maps. Then the range-Doppler maps of all virtual antennas are non-coherently accumulated before applying detection algorithms, like Constant False Alarm Rate (CFAR), to extract potential targets. Finally, the targets' direction of arrival (DoA) is estimated by applying FFT on the antenna dimension. Although the radar point cloud density can be improved by the non-coherent accumulation, which enhances the signal-to-noise ratio of weak reflective targets, its Doppler's estimation bias can be passed to the DoA estimation, degrading the accuracy of the radar point cloud. Moreover, the FFT-based pipeline is hampered by sidelobe noise and low resolution from angle FFT, which further limits the SLAM performance.

Evolving from the FFT method, this paper proposes a novel digital beamforming-based pipeline to process raw radar data, significantly improving the precision of radar points and consequently the accuracy of radar-based 3D SLAM systems. Our main contributions are as follows:

- A novel radar signal processing pipeline that integrates advanced spatial domain beamforming techniques and extends them to 3D DoA estimation.
- Extensive experiments on both filter and graph based radar odometry methods, demonstrating substantial accuracy gain on both radar localization and mapping by replacing the FFT pipeline.

II. METHODOLOGY

A. System Overview

The proposed radar signal processing pipeline is illustrated in Figure 2. Different from the frequency domain based traditional pipeline, our pipeline is based on the spatial domain. 1D FFT is firstly conducted on the fast time dimension (Section II-B). Then, the DoA beamforming is performed on the range-FFT results to estimate the DoA of potential targets in the environment (Section II-C). Given the DoA information, all radar echoes are coherently accumulated and FFT is performed on the slow time dimension to estimate the Doppler of the corresponding targets (Section II-D).

B. MIMO Radar Signal Model

Based on the concept and principles of 2D MIMO radar in [24], we derive the 3D MIMO radar signal model in a more general form. As shown in Figure 3, a typical MIMO radar system consists of multiple virtual antennas along X-axis (azimuth dimension) and Y-axis (elevation dimension). The potential targets are modeled as single point scatterers in the environment. These scatterers are located at the positive Y-axis (range dimension) and have different DoA and Doppler.

The traditional MIMO radar signal model usually uses trigonometric functions to describe the DoA relationship between the virtual antennas and the scatterers. However, this representation makes the formulation of the radar signal model more complex and less intuitive for programming. In this work, the DoA of the n -th scatterer is represented by a three-dimensional (3D) unit vector as

$$\mathbf{r}_n = [\mu_n \quad \sqrt{1 - \mu_n^2 - v_n^2} \quad v_n]^\top, \quad \mu_n^2 + v_n^2 \leq 1 \quad (1)$$

where μ_n and v_n are the one-dimensional parameters in the domain of real numbers. Note that μ_n and v_n are not the commonly used azimuth ϕ_n and elevation θ_n angles. They can be converted to the real azimuth and elevation angles by

$$\begin{aligned} \theta_n &= \sin^{-1}(v_n), \\ \phi_n &= \sin^{-1}\left(\mu_n / \sqrt{1 - v_n^2}\right). \end{aligned} \quad (2)$$

Given the m -th virtual antenna position \mathbf{d}_m , the phase difference between the reference antenna and the m -th virtual antenna can be calculated by

$$\Delta\varphi_{n,m} = 2\pi\mathbf{r}_n^\top \mathbf{d}_m / \lambda, \quad (3)$$

where λ is the wavelength of the radar signal.

Now we define the steering vector of the n -th scatterer as

$$\mathbf{a}_n = \mathbf{a}(\mu_n, v_n) = [e^{j\Delta\varphi_{n,1}} \quad e^{j\Delta\varphi_{n,2}} \quad \dots \quad e^{j\Delta\varphi_{n,M}}]^\top, \quad (4)$$

where M is the total number of virtual antennas. The steering vector \mathbf{a}_n represents the phase shifts of the n -th scatterer observed across the array elements. Then, the received signal of all virtual antennas \mathbf{x}_n for the n -th scatterer at the k -th time index can be represented as $\mathbf{x}_n(k) = \mathbf{a}_n s_0(k)$, where $s_0(k)$ is the transmitted signal from the target.

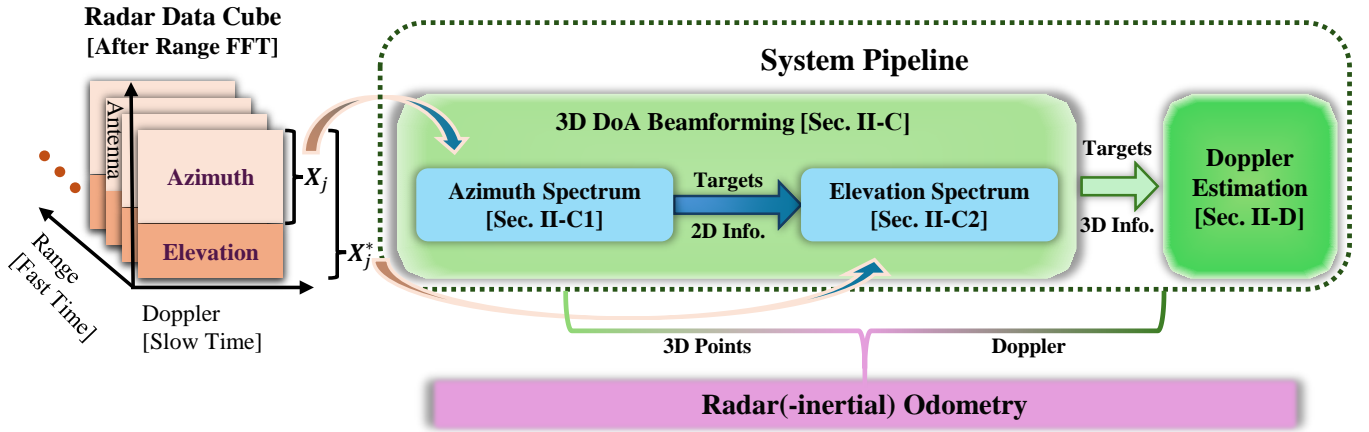


Fig. 2: System overview of the proposed pipeline.

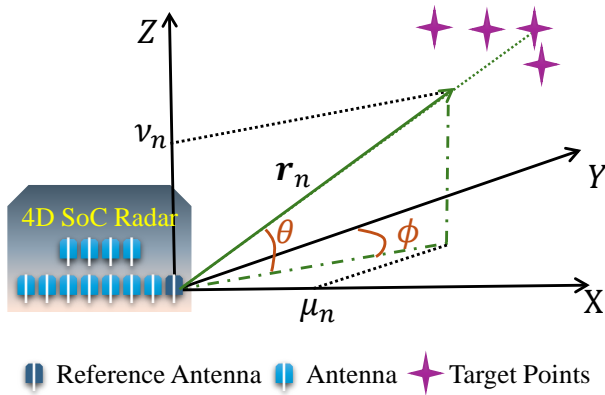


Fig. 3: MIMO radar geometric model.

C. DoA Beamforming

After the range-FFT [25], we estimate the DoA of the potential targets in the spatial domain using beamforming techniques. We propose to use a minimum variance distortionless response (MVDR or Capon) beamforming algorithm [26] as the baseline, and further extend it to 3D DoA estimation problem.

1) *Azimuth*: A two-step DoA estimation algorithm is presented in this work, as illustrated in Figure 2. First, we estimate the DoA of potential targets in the azimuth dimension. It is generally assumed that the DoA of all targets relative to the radar remains unchanged within a single frame. The received signal of all virtual antennas within the frame can be represented as

$$\mathbf{X} = \sum_{n=1}^N [\mathbf{x}_n(1) \quad \mathbf{x}_n(2) \quad \dots \quad \mathbf{x}_n(K)]^T, \quad (5)$$

where N is the total number of potential targets in the frame, K is the total number of time indexes in the frame, and $\mathbf{X} \in \mathbb{R}^{M \times K}$ is the received signal matrix.

It can be seen from Eq. 5 that the received signals from all targets are superimposed. To separate the signal from different targets, we traverse simultaneously in both azimuth and range dimensions to calculate the power spectrum of

each azimuth bin and range bin. Define the self-covariance matrix of the received signal at the j -th range bin as

$$\mathbf{R}_{jj} = \mathbf{X}_j \mathbf{X}_j^H / K, \quad (6)$$

where H operation is the conjugate transpose, and \mathbf{X}_j is the 2D slice of radar data cube at the j -th range bin. Then, the Capon spectrum power $P(\mu)$ of an azimuth bin μ in one range bin can be calculated as

$$P(\mu) = \frac{1}{\mathbf{a}^H(\mu, v) \mathbf{R}_{jj}^{-1} \mathbf{a}(\mu, v)}, \quad \text{for } v = 0. \quad (7)$$

Note that only virtual antennas with zero elevation angle are used in this step. We repeat the above process for all azimuth bins and range bins, which generates a 2D Capon spectrum power map, also known as a range-azimuth map. As the range-azimuth map shown in Figure 4a, the pixel color represents the power of the corresponding azimuth and range. A brighter pixel indicates a higher possibility of one or more strong reflection points in the corresponding azimuth and range. To extract these potential targets, we apply OS-CFAR detection [27] on the range-azimuth map and obtain a set of azimuth candidates $\Theta = \{(\mu_1), (\mu_2), \dots, (\mu_N)\}$ for all potential targets.

2) *Elevation*: Given the set of potential targets Θ , we estimate the elevation of each target in the second step using all virtual antennas. For the candidate target (μ_n) , the self-covariance matrix \mathbf{R}_{jj}^* is recalculated using Eq. 6, which incorporates additional virtual antennas with non-zero elevation angle. Then, we sweep all possible elevation angles v and calculate the corresponding Capon spectrum power $P(\mu_n, v)$. The Capon spectrum power of the l -th elevation bin v_l can be calculated as

$$\begin{cases} P(\mu_n, v_l) = \frac{1}{\mathbf{a}^H(\mu_n, v_l) \mathbf{R}_{jj}^{*-1} \mathbf{a}(\mu_n, v_l)} \\ \mathbf{w}(\mu_n, v_l) = \frac{\mathbf{R}_{jj}^{*-1} \mathbf{a}(\mu_n, v_l)}{\mathbf{a}^H(\mu_n, v_l) \mathbf{R}_{jj}^{*-1} \mathbf{a}(\mu_n, v_l)} \end{cases}, \quad (8)$$

where $\mathbf{w}(\mu_n, v_l)$ is the Capon beamforming weight vector.

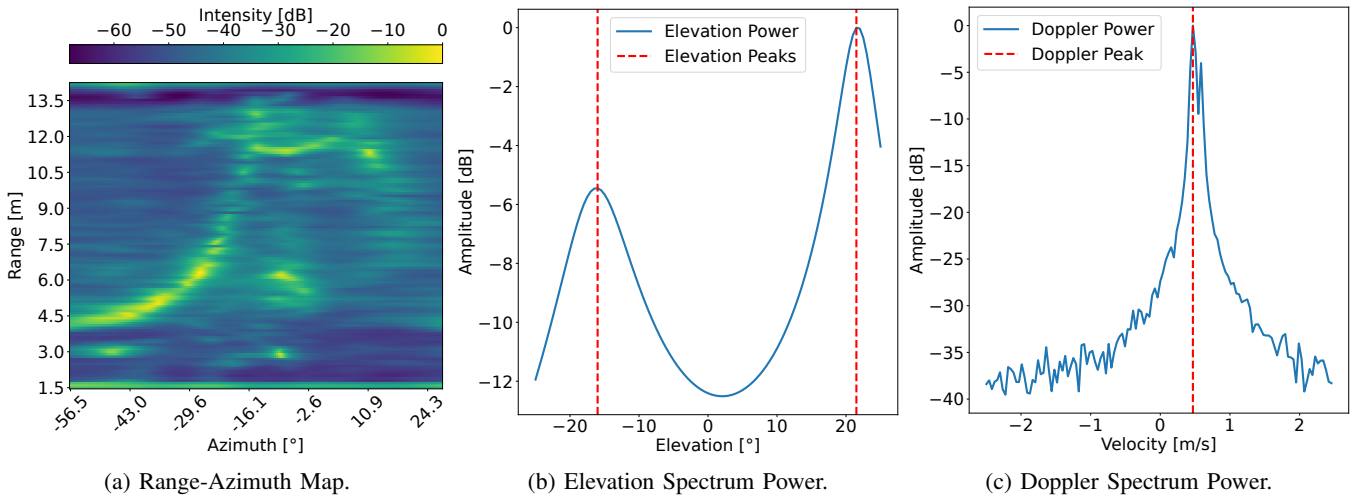


Fig. 4: DoA estimation and Doppler estimation.

Parameter	Value
Max Azimuth Angular	$\pm 70^\circ$
Max Elevation Angular	$\pm 25^\circ$
Azimuth Bin Number	188
Elevation Bin Number	101
Azimuth Virtual Antenna number	8
Elevation Virtual Antenna number	4

TABLE I: Parameter Specifications

An example of the Capon spectrum power in the elevation dimension is shown in Figure 4b. The 2D curve in the figure represents the beamforming results over all possible elevation angles at a given range and azimuth angle. The peak of the curve indicates the most probable elevation angle of the target. Note that there may be multiple peaks in the curve, which is caused by the multiple targets at the same range and azimuth. So we extract all the local maximum peaks in the curve as the elevation angles of the potential targets. So far, we have obtained the DoA of all potential targets $\Theta = \{(\mu_1, \nu_1), (\mu_2, \nu_2), \dots, (\mu_N, \nu_N)\}$.

D. Doppler Estimation

After the DoA estimation, we estimate the Doppler of all targets. Given the DoA of the n -th target (μ_n, ν_n) , we need to suppress the interference of other targets. This can be achieved by applying the Capon beamforming on the \mathbf{X}_j^* using the Capon beamforming weight vector $\mathbf{w}(\mu_n, \nu_n)$. The beamforming results of the n -th target is

$$\mathbf{x}_n = \mathbf{w}^H(\mu_n, \nu_n) \mathbf{X}_j^* \quad (9)$$

where $\mathbf{x}_n \in \mathbb{R}^{1 \times K}$ only contains the Doppler information of the n -th target. Then 1D FFT is applied on \mathbf{x}_n to estimate the Doppler of the n -th target. The Doppler spectrum power of the n -th target is given by

$$P_n = |\text{FFT}(x_n)|. \quad (10)$$

We can now find the maximum of the Doppler spectrum power by $V_{\text{Doppler}} = \arg \max_V P_n(V)$ as the target's estimated radial velocity V_{Doppler} , as the example shown in Figure 4c.

TABLE II: Chamfer Distance for all point clouds [m]

Res.	Mode	Sequence			
		hallways0	outdoors0	aspen11	army2
0.2	Ours	0.14560	0.15477	0.16951	0.15622
	FFT	0.16443	0.15828	0.17146	0.16803
0.1	Ours	0.05194	0.05834	0.06198	0.05277
	FFT	0.06566	0.06308	0.07320	0.06703
0.05	Ours	0.01945	0.02162	0.02333	0.01831
	FFT	0.02477	0.02418	0.02733	0.02475
0.02	Ours	0.00322	0.00381	0.00646	0.00346
	FFT	0.00421	0.00440	0.00699	0.00453
0.01	Ours	0.00065	0.00072	0.00154	0.00072
	FFT	0.00084	0.00085	0.00168	0.00090

Given these detected 3D target points and their associated Doppler velocities, we propose to use them, as more accurate replacements for those generated from the standard FFT-based pipeline, with radar odometry/SLAM algorithms.

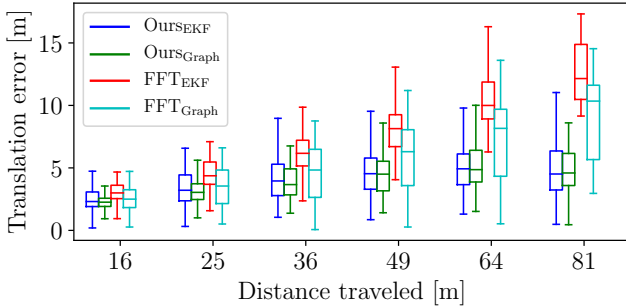
III. EXPERIMENTS

A. Experimental Setup

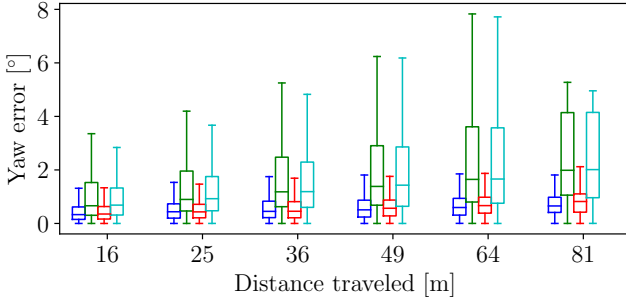
To evaluate the performance of the proposed framework, we conduct a series of experiments on the public ColoRadar dataset [28]. The raw radar data in the dataset is used to evaluate the performance. The raw radar data is collected by a single-chip SoC radar (Texas Instruments AWR1843BOOST-EVM paired with a DCA1000EVM). The proposed pipeline processes the raw radar data to generate an accurate radar point cloud (called our point cloud). The radar point clouds, provided by the ColoRadar dataset, are generated by the traditional FFT pipeline (called FFT point cloud). These two different pipelines are compared in four different sequences: ec_hallways_run0, outdoors_run0, aspen_run11, and edgar_army_run2, which contains indoor and outdoor scenes, structural and unstructured scenes. Key parameters of the proposed pipeline are shown in Table I. We do not compare learning-based methods in this work, as they can not provide

TABLE III: Drift with per distance and APE (RMSE) for each sequence. Red highlights the best result on each sequence.

Sequence	RIO	Point cloud	Drift with per distance				APE (RMSE)		
			XYZ[m][%]	XY[m][%]	Z[m][%]	Yaw[°][°/m]	Trans. [m]	Yaw[°]	
outdoors0 115.4m	Graph	Ours	5.658 [4.9]	0.473 [0.4]	5.638 [4.8]	1.140 [0.010]	1.807	0.158	
		FFT	6.087 [5.2]	1.327 [1.1]	5.940 [5.1]	0.984 [0.009]	2.377	0.093	
	EKF	Ours	1.513 [1.3]	0.542 [0.4]	1.413 [1.2]	0.816 [0.007]	0.678	0.172	
		FFT	13.426 [11.6]	3.210 [2.7]	13.037 [11.2]	0.892 [0.008]	4.314	0.172	
aspens11 78.9m	Graph	Ours	7.791 [9.8]	0.161 [0.2]	7.789 [9.8]	0.482 [0.006]	2.488	0.144	
		FFT	5.482 [6.9]	0.883 [1.1]	5.410 [6.8]	0.493 [0.006]	1.704	0.101	
	EKF	Ours	6.821 [8.6]	0.301 [0.3]	6.815 [8.6]	0.318 [0.004]	2.264	0.149	
		FFT	10.768 [13.6]	0.992 [1.2]	10.722 [13.5]	0.580 [0.007]	3.314	0.133	
army2 129.2m	Graph	Ours	2.959 [2.2]	2.368 [1.8]	1.775 [1.3]	0.400 [0.003]	1.281	0.149	
		FFT	18.889 [14.5]	1.041 [0.8]	18.861 [14.5]	0.825 [0.006]	6.114	0.122	
	EKF	Ours	5.724 [4.4]	1.483 [1.1]	5.528 [4.2]	1.384 [0.011]	2.051	0.209	
		FFT	23.159 [17.8]	0.796 [0.6]	23.145 [17.8]	0.602 [0.005]	7.359	0.157	
hallways0 111.4m	Graph	Ours	1.980 [1.7]	0.650 [0.5]	1.870 [1.6]	0.402 [0.004]	1.450	0.167	
		FFT	15.488 [13.8]	2.103 [1.8]	15.344 [13.7]	0.398 [0.004]	4.667	0.159	
	EKF	Ours	1.360 [1.2]	0.883 [0.7]	1.035 [0.9]	1.561 [0.014]	1.337	0.171	
		FFT	15.879 [14.2]	1.423 [1.2]	15.815 [14.1]	1.925 [0.017]	5.007	0.162	



(a) Translation



(b) Rotation

Fig. 5: Boxplot of the RPE in all sequences.

the Doppler information of the radar point cloud, which is essential for radar-inertial odometry.

B. Point Precision

In order to analyze the point precision, we first generate groundtruth environmental point clouds by projecting all LiDAR point clouds into the global frame. Then we project the FFT and our radar point clouds using the provided groundtruth poses and the extrinsic parameters between radar and Vicon. The Chamfer Distance [29] is calculated using the

estimated point cloud and the groundtruth point cloud. The result is shown in Table II. The parameter Res. represents the resolution level of the point clouds, affecting the density of detected points before Chamfer Distance computation.

In all scenes and resolutions, our point clouds have a smaller Chamfer Distance value than the FFT point clouds. This metric decreased by 1.14% to 26.02%, with an average decrease of 14.70%. A smaller value of Chamfer Distance indicates that the estimated point cloud has a smaller error to the groundtruth point cloud. Thus, our point cloud is closer to the groundtruth point cloud in all scenes and resolutions. This result demonstrates that the proposed pipeline can generate more accurate point clouds than the traditional FFT pipeline.

C. Odometry Accuracy

To further evaluate the influence of the proposed pipeline on a full radar-inertial odometry system, we select two different radar-inertial odometry systems as the baseline, and compare their localization accuracy incorporating different radar signal processing pipelines. The first system is a filter-based radar-inertial odometry [14]. It calculates the ego-velocity of a single frame using Doppler information of all radar point clouds within this frame, and then fuses the ego-velocity with the IMU data in an Extended Kalman Filter to estimate the pose. The second system is the graph-based radar-inertial odometry [15]. Rather than calculating the ego-velocity of a single frame, it directly uses the Doppler information of single radar point as the edge in the graph, and then optimizes the pose and velocity of all frames in a fixed lag sliding window. These two radar-inertial odometry systems stand for the two main fusion strategies in radar-inertial odometry.

To make a fair comparison, we only adjust the radar-related parameters in these two systems, and keep all other parameters unchanged. The barometer fusion strategy is not activated in both systems, due to the lack of barometer data

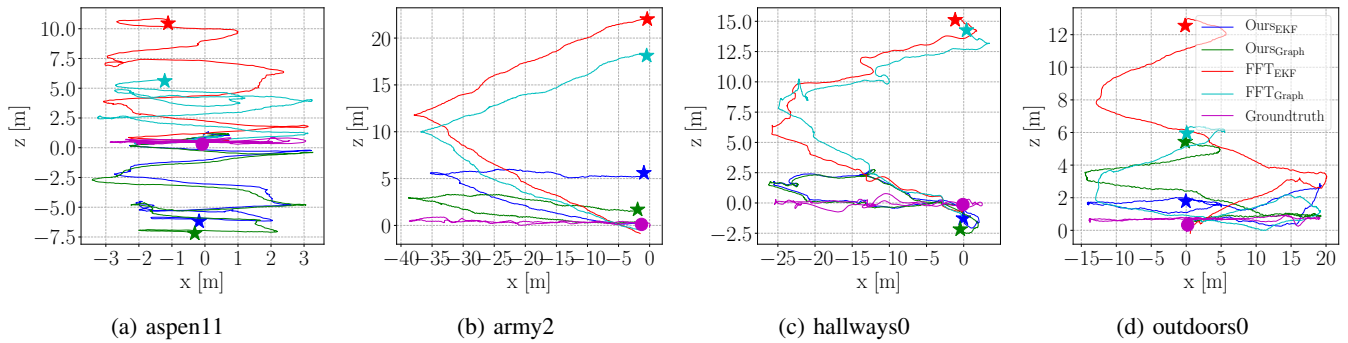


Fig. 6: Side view of all trajectories in the XZ-plane of all sequences. The dots represent the starting positions, while the pentagrams represent the end positions. The displacement between them indicates the degree of drift in each trajectory.

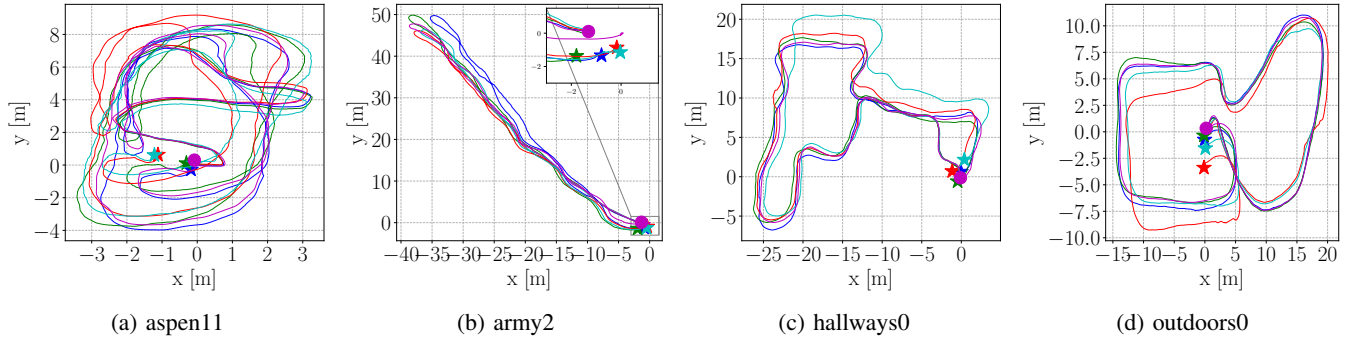


Fig. 7: Top view of all trajectories in the XY-plane of all sequences. The colors of the trajectories, as well as dots and pentagrams, are consistent with those used in the previous figures.

in the ColoRadar dataset. We evaluate the odometry accuracy using the Absolute Pose Error (APE) and Relative Pose Error (RPE) metrics [30]. The statistics are shown in Table III. The boxplot of the RPE summarized in all sequences are shown in Figure 5.

It can be seen that the proposed pipeline can significantly improve the localization performance of different radar-inertial odometry systems in different scenes. The translation error decreases by 1.62% to 22.07%, with an average decrease of 13.68%. The rotation error does not have a significant change. This may be due to the fact that these two radar-inertial odometry systems mainly use the Doppler information, rather than the structure information. The Doppler information mostly affects the translation estimation and has less impact on the rotation estimation. Thus, even though the proposed pipeline can generate more accurate point clouds, Doppler-only update strategy in these two systems may not fully utilize the improved point clouds, which needs further investigation.

To further analyze the odometry accuracy, we visualize the estimated trajectories in the XZ-plane and XY-plane, as shown in Figure 6 and Figure 7. In the both XY-plane and XZ-plane, the estimated trajectories based on the proposed pipeline are closer to the groundtruth. The first reason is that the proposed pipeline mainly focuses on extracting the stable and strong reflection points in the radar signal while ignoring the noisy and weak reflection points. This characteristic can

decrease the possibility of generating outliers or noise points in the radar point cloud, which in turn can improve the odometry accuracy. The second reason is traditional FFT pipeline needs to compensate for the Doppler estimation before the DoA estimation, which may introduce additional errors in the DoA estimation. Furthermore, the single-chip radar used in the ColoRadar dataset only has two virtual elevation antennas, which further exacerbates the traditional pipeline elevation errors. This could explain why the proposed pipeline can significantly decrease the Z-axis drift in the estimated trajectory, as shown in Figure 6.

IV. CONCLUSION

In this paper, we design a novel radar signal processing pipeline. Taking full advantage of the digital beamforming techniques, the proposed pipeline can generate more accurate 3D radar point clouds than traditional FFT-based pipelines. The proposed pipeline is evaluated on the public ColoRadar dataset, and the results show that the proposed pipeline can significantly decrease the error of the radar point clouds, and further improve the accuracy of radar-inertial odometry systems. This paper highlights the significance of utilizing raw radar signals from a single-chip radar to enhance the localization and mapping accuracy in radar-inertial odometry systems. This approach is akin to designing more advanced feature extraction algorithms for visual odometry/SLAM. Future research can focus on improving the rotation estimation accuracy.

REFERENCES

- [1] K. Zhang, Y. Ding, S. Xu, Z. Hong, X. Kong, and S. Wang, "CURL-MAP: Continuous Mapping and Positioning with CURL Representation†," in *2024 IEEE International Conference on Robotics and Automation (ICRA)*, May 2024, pp. 8580–8586.
- [2] J. Jiang, J. Yuan, X. Zhang, and X. Zhang, "DVIO: An Optimization-Based Tightly Coupled Direct Visual-Inertial Odometry," *IEEE Transactions on Industrial Electronics*, vol. 68, no. 11, pp. 11 212–11 222, Nov. 2021.
- [3] A. Venon, Y. Dupuis, P. Vasseur, and P. Merriaux, "Millimeter Wave FMCW RADARs for Perception, Recognition and Localization in Automotive Applications: A Survey," *IEEE Transactions on Intelligent Vehicles*, vol. 7, no. 3, pp. 533–555, Sept. 2022.
- [4] K. Harlow, H. Jang, T. D. Barfoot, A. Kim, and C. Heckman, "A New Wave in Robotics: Survey on Recent mmWave Radar Applications in Robotics," Jan. 2024.
- [5] Z. Hong, Y. Petillot, A. Wallace, and S. Wang, "RadarSLAM: A robust simultaneous localization and mapping system for all weather conditions," *The International Journal of Robotics Research*, vol. 41, no. 5, pp. 519–542, Apr. 2022.
- [6] D. Adolphsson, M. Magnusson, A. Alhashimi, A. J. Lilienthal, and H. Andreasson, "Lidar-level localization with radar? the cfear approach to accurate, fast, and robust large-scale radar odometry in diverse environments," *IEEE Transactions on robotics*, vol. 39, no. 2, pp. 1476–1495, 2023.
- [7] Y. S. Park, Y.-S. Shin, and A. Kim, "PhaRaO: Direct Radar Odometry using Phase Correlation," in *2020 IEEE International Conference on Robotics and Automation (ICRA)*. IEEE, May 2020, pp. 2617–2623.
- [8] A. Mock, M. Magnusson, and J. Hertzberg, "RadaRays: Real-time Simulation of Rotating FMCW Radar for Mobile Robotics via Hardware-accelerated Ray Tracing," p. 2470–2477, Mar. 2025.
- [9] Z. Han, J. Wang, Z. Xu, S. Yang, L. He, S. Xu, J. Wang, and K. Li, "4D Millimeter-Wave Radar in Autonomous Driving: A Survey," Feb. 2024.
- [10] C. Doer and G. F. Trommer, "X-RIO: Radar Inertial Odometry with Multiple Radar Sensors and Yaw Aiding," *Gyroscopy and Navigation*, vol. 12, no. 4, pp. 329–339, Dec. 2021.
- [11] J.-T. Huang, R. Xu, A. Hinduja, and M. Kaess, "Multi-Radar Inertial Odometry for 3D State Estimation using mmWave Imaging Radar," in *2024 IEEE International Conference on Robotics and Automation (ICRA)*, May 2024, pp. 12 006–12 012.
- [12] V. Kubelka, E. Fritz, and M. Magnusson, "Do we need scan-matching in radar odometry?" in *2024 IEEE International Conference on Robotics and Automation (ICRA)*, 2024, pp. 13 710–13 716.
- [13] Q. Huang, Y. Liang, Z. Qiao, S. Shen, and H. Yin, "Less is More: Physical-Enhanced Radar-Inertial Odometry," in *2024 IEEE International Conference on Robotics and Automation (ICRA)*, May 2024, pp. 15 966–15 972.
- [14] C. Doer and G. F. Trommer, "An EKF Based Approach to Radar Inertial Odometry," in *2020 IEEE International Conference on Multisensor Fusion and Integration for Intelligent Systems (MFI)*. IEEE, Sept. 2020, pp. 152–159.
- [15] R. Girod, M. Hauswirth, P. Pfreundschuh, M. Biasio, and R. Siegwart, "A robust baro-radar-inertial odometry m-estimator for multicopter navigation in cities and forests," in *IEEE Int. Conf. Multisensor Fusion Integration Intell. Syst.*, Aug. 2024.
- [16] J. Zhang, H. Zhuge, Z. Wu, G. Peng, M. Wen, Y. Liu, and D. Wang, "4DRadarSLAM: A 4D Imaging Radar SLAM System for Large-scale Environments based on Pose Graph Optimization," in *2023 IEEE International Conference on Robotics and Automation (ICRA)*. IEEE, May 2023, pp. 8333–8340.
- [17] H. Chen, Y. Liu, and Y. Cheng, "DRIO: Robust Radar-Inertial Odometry in Dynamic Environments," *IEEE Robotics and Automation Letters*, vol. 8, no. 9, pp. 5918–5925, Sept. 2023.
- [18] A. Prabhakara, T. Jin, A. Das, G. Bhatt, L. Kumari, E. Soltanaghaj, J. Bilmes, S. Kumar, and A. Rowe, "High Resolution Point Clouds from mmWave Radar," in *2023 IEEE International Conference on Robotics and Automation (ICRA)*. IEEE, May 2023, pp. 4135–4142.
- [19] R. Zhang, D. Xue, Y. Wang, R. Geng, and F. Gao, "Towards Dense and Accurate Radar Perception Via Efficient Cross-Modal Diffusion Model," *IEEE Robotics and Automation Letters*, Mar. 2024.
- [20] Y. Cheng, J. Su, M. Jiang, and Y. Liu, "A Novel Radar Point Cloud Generation Method for Robot Environment Perception," *IEEE Transactions on Robotics*, vol. 38, no. 6, pp. 3754–3773, Dec. 2022.
- [21] Z. Zeng, X. Dang, Y. Li, X. Bu, and X. Liang, "Angular Super-Resolution Radar SLAM," in *2021 IEEE/RSJ International Conference on Intelligent Robots and Systems (IROS)*, Sept. 2021, pp. 5456–5461.
- [22] P. Meiresone, D. Van Hamme, W. Philips, and T. Verbelen, "Ego-motion estimation with a lowpower millimeterwave radar on a UAV," in *International Conference on Radar Systems (RADAR 2022)*, vol. 2022, Oct. 2022, pp. 371–376.
- [23] I. Bilik, O. Longman, S. Villeval, and J. Tabrikian, "The Rise of Radar for Autonomous Vehicles: Signal Processing Solutions and Future Research Directions," *IEEE Signal Processing Magazine*, vol. 36, no. 5, pp. 20–31, Sept. 2019.
- [24] S. Rao, "MIMO Radar," Texas Instruments, Application Report SWRA554A, July 2018.
- [25] C. Iovescu and S. Rao, "The fundamentals of millimeter wave radar sensors," *Texas Instruments*, 2017.
- [26] A. Ślesicka, A. Kawalec, and B. Ślesicki, "Capon-like method for direction of arrival estimation using TDM MIMO radar," *Metrology and Measurement Systems*, pp. 481–497, June 2023.
- [27] H. Rohling, "Ordered statistic CFAR technique - an overview," in *2011 12th International Radar Symposium (IRS)*, Sept. 2011, pp. 631–638.
- [28] A. Kramer, K. Harlow, C. Williams, and C. Heckman, "ColoRadar: The direct 3D millimeter wave radar dataset," *The International Journal of Robotics Research*, vol. 41, no. 4, pp. 351–360, Apr. 2022.
- [29] J. Jiao, H. Wei, T. Hu, X. Hu, Y. Zhu, Z. He, J. Wu, J. Yu, X. Xie, H. Huang, R. Geng, L. Wang, and M. Liu, "FusionPortable: A Multi-Sensor Campus-Scene Dataset for Evaluation of Localization and Mapping Accuracy on Diverse Platforms," in *2022 IEEE/RSJ International Conference on Intelligent Robots and Systems (IROS)*, Oct. 2022, pp. 3851–3856.
- [30] Z. Zhang and D. Scaramuzza, "A Tutorial on Quantitative Trajectory Evaluation for Visual(-Inertial) Odometry," in *2018 IEEE/RSJ International Conference on Intelligent Robots and Systems (IROS)*, Oct. 2018, pp. 7244–7251.